J. Fluid Mech. (2009), *vol.* 618, *pp.* 13–39.
doi:10.1017/S0022112008004011 Printed in the United Kingdom

Simulating deformable particle suspensions using a coupled lattice-Boltzmann and finite-element method

ROBERT M. MACMECCAN, J. R. CLAUSEN, G. P. NEITZEL AND C. K. AIDUN†

G. W. Woodruff School of Mechanical Engineering, Georgia Institute of Technology, 500 10th Street NW, Atlanta, GA 30318, USA

(Received 5 October 2007 and in revised form 17 August 2008)

A novel method is developed to simulate suspensions of deformable particles by coupling the lattice-Boltzmann method (LBM) for the fluid phase to a linear finite-element analysis (FEA) describing particle deformation. The methodology addresses the need for an efficient method to simulate large numbers of three-dimensional and deformable particles at high volume fraction in order to capture suspension rheology, microstructure, and self-diffusion in a variety of applications. The robustness and accuracy of the LBM–FEA method is demonstrated by simulating an inflating thin-walled sphere, a deformable spherical capsule in shear flow, a settling sphere in a confined channel, two approaching spheres, spheres in shear flow, and red blood cell deformation in flow chambers. Additionally, simulations of suspensions of hundreds of biconcave red blood cells at 40 % volume fraction produce continuum-scale physics and accurately predict suspension viscosity and the shear-thinning behaviour of blood. Simulations of fluid-filled spherical capsules which have red-blood-cell membrane properties also display deformation-induced shear-thinning behaviour at 40 % volume fraction, although the suspension viscosity is significantly lower than blood.

1. Introduction

Non-dilute suspensions of deformable particles are integral to many industrial and biological processes. Whether the suspended particles are added to the fluid for the sole purpose of modifying the fluid's behaviour such as in paint (Cohu & Magnin 1995), the particles define the industrial product such as fibres in paper making (Thorp & Kocurek 1998), or the particles perform biological functions such as platelets (Goldsmith *et al.* 1995; Kroll *et al.* 1996), leukocytes (Munn, Melder & Jain 1996), and red blood cells (Fung 1993), understanding the underlying physical processes is paramount. In this paper, a novel method based on coupling the lattice-Boltzmann method (LBM) to a linear finite-element analysis (FEA) is developed to allow the simulation of deformable particle suspensions. The methodology addresses the need for an efficient method to simulate large numbers of three-dimensional deformable particles in order to capture suspension rheology, microstructure, and self-diffusion in a variety of applications. Some important suspension properties such as normal stress differences and suspension pressure can

† Author to whom correspondence should be addressed.

be difficult to measure experimentally; however, the fluid and solid states are known in simulations, allowing for easy computation of bulk stress and derivative terms such as suspension pressure and normal stress differences, local microstructure, and particle diffusivities.

Computer simulations including the lattice-Boltzmann method (Ladd 1994; Aidun & Lu 1995; Aidun, Lu & Ding 1998; Qi 1999; Ding & Aidun 2000, 2003; Ladd & Verberg 2001) and Stokesian Dynamics (Brady & Bossis 1988; Sierou & Brady 2002, 2004) have revealed important phenomena in self-diffusion and microstructure anisotropy. Although these simulation techniques have aided understanding of suspension physics, they are unable to capture phenomena unique to deformable suspensions. Existing simulation techniques for deformable particles including the boundary-integral (Breyiannis & Pozrikidis 2000; Zinchenko & Davis 2002; Pozrikidis 2003, 2005) and immersed-boundary methods (Eggleton & Popel 1998; Liu & Liu 2006) have advanced this area considerably. Dupin *et al.* (2007) have applied the LBM to the simulation of deformable particles, and they illustrate the computational efficiency and parallelism the lattice-Boltzmann framework affords.

The coupled LBM–FEA simulation technique developed in this paper allows the efficient simulation of large numbers of deformable particles and leverages the ease of parallel implementation of the lattice-Boltzmann method, fluid–solid coupling, and linear-elastic finite-element description of particle deformation. This paper presents the coupled LBM–FEA methodology in § 2, with consideration to computational efficiency, the FEA object discretization, and stability issues unique to the LBM and FEA coupling. In § 3, several sample simulations are presented in order to validate the methodology to experimental and analytic results, and in § 4, results for large numbers of red blood cells and spherical fluid-filled capsules are shown. The efficiency, versatility, and limitations of this method are discussed in § 5.

2. Method

2.1. *Lattice-Boltzmann*

The lattice-Boltzmann technique is well-documented for the direct numerical simulation of particles suspended in fluid (Ladd 1994; Aidun & Lu 1995; Aidun *et al.* 1998; Qi 1999; Ding & Aidun 2000, 2003, 2006; Ladd & Verberg 2001). Many variants of the LBM exist, but the method of Aidun *et al.* (hereinafter referred to as ALD) is presented here. As initially described by Aidun *et al.*, the ALD method is a single-relaxation method that excludes the fluid inside a solid boundary. This method is suited to moderately low-Reynolds-number flows, whereas other lattice-Boltzmann variants may be used for both zero and higher (Lallemand & Luo 2000) Reynolds-number flows. The lattice-Boltzmann technique is presented here in the non-colloidal limit, where the effect of Brownian motion is negligible. Extensions to Brownian suspensions are possible and have been demonstrated for rigid-particle suspensions (Ladd & Verberg 2001).

Briefly, the lattice-Boltzmann method discretizes the velocity space of the Boltzmann equation, resulting in a lattice spacing based on the chosen set of discrete velocity vectors, $\boldsymbol{e}_{\sigma i}$. A three-dimensional 19-vector Cartesian velocity set is chosen for $\boldsymbol{e}_{\sigma i}$, where the subscripts σ and i denote the Cartesian directions. The time evolution of the Boltzmann particle distribution function is calculated through a collision and streaming operator using the Bhatnagar–Gross–Krook (BGK) collision operator with

a single relaxation time, τ (Chen & Doolen 1998),

$$f_{\sigma i}(\boldsymbol{r}+\boldsymbol{e}_{\sigma i}, t+1) = f_{\sigma i}(\boldsymbol{r}, t) - \frac{1}{\tau}\big(f_{\sigma i}(\boldsymbol{r}, t) - f^{(0)}_{\sigma i}(\boldsymbol{r}, t)\big), \tag{2.1}$$

where $f_{\sigma i}$ is the Boltzmann particle-distribution function, $f^{(0)}_{\sigma i}$ is the equilibrium distribution function, $\boldsymbol{r}$ is the spatial location, and t is the time. The solution to the lattice-Boltzmann equation is obtained at low Mach number based on the lattice-Boltzmann pseudo-sound speed, c_s. As demonstrated using a Chapman–Enskog expansion (McNamara & Zanetti 1988), the lattice-Boltzmann technique converges to the Navier–Stokes equations when the lattice spacing, $c_{\sigma i}$, is much smaller than a characteristic length scale of the simulation. The lattice-Boltzmann relaxation time scale is related to the fluid viscosity by $\tau = 3\nu + 0.5$. The equilibrium distribution function is defined as

$$f^{(0)}_{\sigma i}(\boldsymbol{r}, t) = \rho(\boldsymbol{r}, t)[A_\sigma + B_\sigma(\boldsymbol{e}_{\sigma i}\cdot\boldsymbol{u}) + C_\sigma(\boldsymbol{e}_{\sigma i}\cdot\boldsymbol{u})^2 + D_\sigma u^2], \tag{2.2}$$

where density and momentum are given by

$$\rho(\boldsymbol{r}, t) = \sum_{\sigma, i} f_{\sigma i}(\boldsymbol{r}, t)$$

and

$$\rho(\boldsymbol{r}, t)\boldsymbol{u}(\boldsymbol{r}, t) = \sum_{\sigma, i} f_{\sigma i}(\boldsymbol{r}, t)\,\boldsymbol{e}_{\sigma i}.$$

Mass and momentum must be conserved by the equilibrium distribution function, and coefficients A_σ to D_σ, along with the details of the fluid–solid interaction, are given by Aidun *et al.* (1998). Fluid-particle boundaries are considered in a 'link-bounce-back' manner based on the lattice links crossing a solid boundary as discussed in § 2.3.

2.2. *Finite-element*

The present study examines both deformable solid particles and deformable fluid-filled membranes; however, the framework is general and may incorporate a variety of models. The trajectory and deformation of an elastic deformable solid are governed by Cauchy's equation,

$$\frac{\mathrm{D}\rho_s\boldsymbol{u}_s}{\mathrm{D}t} = \nabla\cdot\boldsymbol{T}, \tag{2.3}$$

in which the left-hand side is the material derivative of solid momentum, and $\boldsymbol{T}$ is the elastic stress tensor. For deformable solid particles, the shearoelastic number (Goddard & Miller 1967; Pal 2003), $N_{se} = \mu\dot{\gamma}/G_S$, governs particle deformation where μ is the fluid dynamic viscosity, $\dot{\gamma}$ is the fluid shear rate, and G_S is the particle shear modulus. The capillary number, $Ca_G = \mu\dot{\gamma}R/G_M$, governs deformation of fluid-filled elastic capsules, where R is the particle radius and G_M is the effective membrane shear modulus ($G_M = G_S t_M$ for membranes with thickness, t_M).

A transient finite-element analysis is chosen to calculate the time evolution of deformable particles in suspension because this method is well developed and versatile. The transient finite-element method integrates virtual work over the volume of the element,

$$\int \mathrm{tr}(\bar{\boldsymbol{\varepsilon}}\otimes\boldsymbol{T})\,\mathrm{d}V = \int \bar{\boldsymbol{X}}\cdot\boldsymbol{F}^{tr}\mathrm{d}A + \int \bar{\boldsymbol{X}}\cdot\boldsymbol{F}^{b}\,\mathrm{d}V, \tag{2.4}$$

where $\bar{\boldsymbol{X}}$ are the elemental virtual displacements, $\bar{\boldsymbol{\varepsilon}}$ is an elemental virtual strain due to virtual displacements, $\boldsymbol{F}^{tr}$ are traction stresses on the surface, $\boldsymbol{F}^{b}$ are body stresses

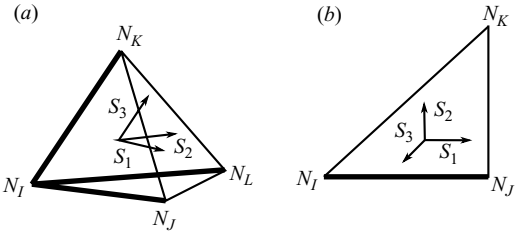

FIGURE 1. (*a*) Linear-elastic solid element with four nodes (tetrahedron) and (*b*) linear-elastic shell element with 3 nodes (triangle). Shell elements have a constant thickness and rotational degrees of freedom along elemental coordinates at each node for bending stiffness.

such as inertia, A is surface area, and V is volume. Nodal displacements and positions are related to elemental displacements and positions through an interpolation or shape function, H_i, by

$$\boldsymbol{X} = \sum_{i=1}^{N} H_i \boldsymbol{x}_i, \quad \boldsymbol{r} = \sum_{i=1}^{N} H_i \boldsymbol{r}_i, \tag{2.5}$$

where $\boldsymbol{r}$ is a global position vector, and $\boldsymbol{x}_i$ and $\boldsymbol{r}_i$ are the nodal displacement and global position vectors of the ith node, respectively. The relationships in (2.5) also hold for virtual displacements, and the summation is over all nodes in a given element. In the present study, linear-elastic solid elements are used to model solid deformable particles such as platelets, and linear-elastic shell elements are used to model deformable fluid-filled membranes such as capsules and red blood cells. The linear-elastic solid element is shown in figure 1(*a*) with four nodes, and the linear-elastic shell element is shown in figure 1(*b*) with three nodes.

The shape function uses a natural coordinate system to express virtual (or actual) displacements of the nodes to any point on an element. These coordinates, $\boldsymbol{S} = (S_1, S_2, S_2)$, are defined in figure 1 with an origin in the centre of the element and normalized such that for any given direction i, $-1 \leqslant S_i \leqslant 1$. For solid elements, the coordinates are not necessarily orthogonal and follow the undeformed element edges, which are shown in bold in figure 1(*a*). The shape function for solid elements is

$$\left.\begin{aligned} H_1 &= \tfrac{1}{8}[(1 - S_1)(1 - S_2)(1 - S_3)], \\ H_2 &= \tfrac{1}{8}[(1 + S_1)(1 - S_2)(1 - S_3)], \\ H_3 &= \tfrac{1}{8}[(1 + S_1)(1 + S_2)(1 - S_3)], \\ H_4 &= \tfrac{1}{8}[(1 - S_1)(1 + S_2)(1 - S_3)], \end{aligned}\right\} \tag{2.6}$$

where the shape function subscripts 1, 2, 3, 4 refer to the nodes I, J, K, L in figure 1(*a*). The shell elements are shown in figure 1(*b*) with three nodes and rotational degrees of freedom for bending stiffness. The shape function for shell elements is formed by truncating the solid shape function and taking $i =$ 1–3 in (2.6), where shape function subscripts 1, 2, 3 refer to the nodes I, J, K in figure 1(*b*). The coordinates are always orthogonal for shell elements where the out-of-plane normal coordinate, S_3, is chosen to make the coordinate system right-handed, and S_2 is orthogonal in the direction of N_K.

Elemental strains are calculated by differentiating the elemental displacements, $\boldsymbol{\varepsilon} = \mathrm{d}\boldsymbol{X}/\mathrm{d}\boldsymbol{r}$, and relating the elemental displacement and position to nodal quantities using (2.5). At this point, the integrals in (2.4) are evaluated in terms of nodal

virtual displacements, and elemental stiffness and mass matrices are constructed from elemental material properties such as density and elasticity. A detailed derivation of this process can be found in Bathe (1996). On summing over all elements in the object, the resulting transient finite-element equation is obtained,

$$\boldsymbol{M}\ddot{\boldsymbol{x}} + \boldsymbol{C}\dot{\boldsymbol{x}} + \boldsymbol{K}\boldsymbol{x} = \boldsymbol{F}, \tag{2.7}$$

which determines the time-evolution of the nodal displacement vector, $\boldsymbol{x}$, and its time derivatives, $\dot{\boldsymbol{x}}$ and $\ddot{\boldsymbol{x}}$, where the nodal-displacement vector is defined as the deformed node location minus the undeformed node location. The global mass, $\boldsymbol{M}$, and stiffness, $\boldsymbol{K}$, matrices are constructed from summing the elemental matrices , and the force vector, $\boldsymbol{F}$, is calculated from traction forces resulting from the fluid–solid coupling as described later.

The damping matrix is chosen as a Rayleigh damping matrix,

$$\boldsymbol{C} = \alpha_D \boldsymbol{M} + \beta_D \boldsymbol{K}, \tag{2.8}$$

where the coefficients α_D and β_D are related to the solid body damping ratios via $\zeta(\omega_n) = 0.5(\alpha_D \omega_n^{-1} + \beta_D \omega_n)$, where ζ is the damping ratio for a given modal circular frequency, ω_n. The Rayleigh damping coefficients are chosen based on the desired damping ratios for given solid material properties. To avoid influencing particle dynamics, damping ratios are chosen such that $\zeta(\omega_n) \ll 1$ for all simulations presented here. A finite-element object contains many discrete modes representing a spectrum of vibrational frequencies, and these frequencies are calculated via a modal analysis in ANSYS using a block Lanczos routine. A review of finite-element modal analysis may be found in Bathe (1996).

The transient finite-element equation (2.7) is solved using Newmark's integration method, where Newmark's equations,

$$\ddot{\boldsymbol{x}}_{t+1} = \beta_n^{-1} \Delta t^{-2} [\boldsymbol{x}_{t+1} - \boldsymbol{x}_t - \Delta t \dot{\boldsymbol{x}}_t - \Delta t^2 (0.5 - \beta_n) \ddot{\boldsymbol{x}}_t] \tag{2.9}$$

and

$$\dot{\boldsymbol{x}}_{t+1} = \dot{\boldsymbol{x}}_t + \Delta t [(1 - \gamma_n) + \gamma_n \ddot{\boldsymbol{x}}_{t+1}], \tag{2.10}$$

combine with (2.7) to produce a solid phase time-evolution equation of the form

$$\boldsymbol{K}'_{t+1} \boldsymbol{x}_{t+1} = \boldsymbol{F}'_{t+1}, \tag{2.11}$$

where

$$\boldsymbol{K}' = \boldsymbol{K} + \frac{1}{\beta_n \Delta t^2} \boldsymbol{M} + \frac{\gamma_n}{\beta_n \Delta t} \boldsymbol{C},$$

$$\boldsymbol{F}' = \boldsymbol{F} + \frac{\boldsymbol{M}}{\beta_n \Delta t^2} [\boldsymbol{x}_t + \Delta t \dot{\boldsymbol{x}}_t + \Delta t^2 (0.5 - \beta_n) \ddot{\boldsymbol{x}}_t] + \boldsymbol{C} \left[\frac{\gamma_n}{\beta_n \Delta t} \boldsymbol{x}_t + \left(\frac{\gamma_n}{\beta_n} - 1 \right) \dot{\boldsymbol{x}}_t + \Delta t \left(0.5 \frac{\gamma_n}{\beta_n} - 1 \right) \ddot{\boldsymbol{x}}_t \right], \tag{2.12}$$

and the t subscripts denote time. For convenience, (2.12) is rewritten as $\boldsymbol{F}' = \boldsymbol{F} + \boldsymbol{M}' + \boldsymbol{C}'$. The choice of $\beta_n = 1/6$ and $\gamma_n = 1/2$ yields a constant acceleration method that is unconditionally stable. To guarantee convergence, the integration time step, Δt, is chosen as less than 0.1 of the smallest fundamental period as determined by the modal analysis of the finite-element particle. In general, finite-element integration may be performed on a different time scale from the lattice-Boltzmann propagation and collision. For example, FEA integration can be performed every 10 lattice-Boltzmann

time steps to optimize computational efficiency. For particle shearoelastic or capillary numbers $O(0.1)$, the required finite-element time steps are generally longer than the lattice time step; however, in current calculations, the finite-element time step is equal to the lattice time step with a minimal reduction in performance.

In order to simulate large numbers of deformable particles in suspension, the FEA must be incorporated efficiently, necessitating the assumption of small body-fixed deformations. To comply with this assumption, a particle coordinate system is fixed on a particle's centre of mass and oriented using the average angular displacement of the finite-element nodes. Although elemental co-rotational procedures are typically used for large-rotation problems (Rankin & Brogan 1986; Campanelli, Berzeri & Shabana 2000), when averaged, the co-rotational procedure gives less consistent results than a simple average angular displacement. The use of a body-fixed coordinate system for the solid particles results in invariant linear-elastic stiffness, mass and damping matrices that may be determined *a priori* for each type of particle. Thus, the left-hand side of (2.11) is constructed and inverted once for each particle type and applied to all particles of that type at all time steps. This simplification results in $O(n^2)$ operations for the time-evolution of solid particles as opposed to $O(n^3)$ operations for inversion, where n is the size of the particle's finite-element matrices.

2.3. *Fluid–solid coupling*

Coupling between fluid and solid is based on lattice links crossing the solid boundary. These lattice links lie along lattice-direction vectors and have endpoints on lattice nodes on either side of the particle boundary (Aidun *et al.* 1998). Lattice links are found on the discretized finite-element surface using a ray-tracing algorithm commonly used in computer graphics. In this method, rays are projected along the lattice directions and tested for intersection with the triangles comprising the solid surface using a fast and minimum-storage algorithm. The intersection is found through direct three-dimensional calculation using barycentric coordinates, which eliminates the need for two-dimensional projections or calculation of the plane equation for the triangle. For more details on this method, see the implementation by Möller & Trumbore (1997).

The fluid force on the moving solid boundary is determined by

$$F_{\sigma i}^{(B)}\left(\boldsymbol{r}+\tfrac{1}{2}\boldsymbol{e}_{\sigma i'},t+\tfrac{1}{2}\right)=2\boldsymbol{e}_{\sigma i'}[f_{\sigma i'}(\boldsymbol{r},t^{+})-\rho B_{\sigma}\boldsymbol{u}_{b}\cdot\boldsymbol{e}_{\sigma i'}], \tag{2.13}$$

where $F_{\sigma i}^{(B)}$ is the force along the σith lattice direction vector ($\boldsymbol{e}_{\sigma i}$). Lattice vectors with a $\sigma i'$ subscript have opposite directions from lattice vectors with subscript σi, and $f_{\sigma i'}(\boldsymbol{r},t^{+})$ is the post-collision particle-distribution function in the direction $\sigma i'$, where the post-collision particle distribution is defined as

$$f_{\sigma i}(\boldsymbol{r},t^{+})\equiv f_{\sigma i}-\frac{1}{\tau}\left(f_{\sigma i}(\boldsymbol{r},t)-f_{\sigma i}^{(0)}(\boldsymbol{r},t)\right).$$

The boundary velocity, $\boldsymbol{u}_b$, is determined by linear interpolation from the finite-element nodal velocity on the surface intersected by the link. The fluid particle-distribution function along the σith lattice vector is modified by the presence of the solid boundary by

$$f_{\sigma i}(\boldsymbol{r},t+1)=f_{\sigma i'}(\boldsymbol{r},t^{+})+2\rho\beta_{\sigma}\boldsymbol{u}_{b}\cdot\boldsymbol{e}_{\sigma i}, \tag{2.14}$$

which imposes the correct velocity gradient in the fluid stress tensor.

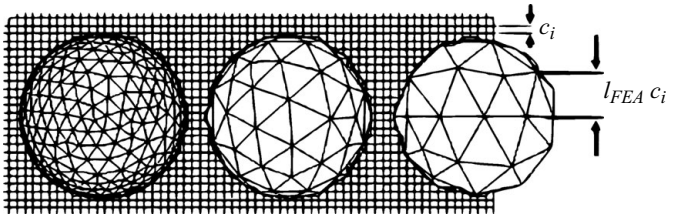

FIGURE 2. Description of spherical particles with elemental mesh length ratios ranging from $l_{FEA} = 2.0$ (finely meshed) to $l_{FEA} = 6.2$ (coarsely meshed). $D = 20$ for all 3 particles.

2.4. *Coupling of forces to finite elements*

The lattice-Boltzmann methodology places restrictions on the ratio of the macroscopic length scale (such as particle diameter, D) and the lattice length scale, $c_{\sigma i}$. This restriction comes from the Knudsen-number-like parameter in the lattice-Boltzmann derivation that requires sufficient lattice resolution of the suspended particles, i.e. $D/c_{\sigma i} \gg 1$. Ding & Aidun (2003) find converging drag on a three-dimensional sphere in a channel for $D > 16$ lattice units, and Ladd (1994) finds good agreement with two-dimensional pressure-driven flow in a channel for widths above 9 lattice units. When the lattice fluid is coupled to a discretized finite-element object, the ratio l_{FEA} is introduced, which is defined as the average finite-element edge length divided by $c_{\sigma i}$. The introduction of this secondary length scale has not been previously investigated and requires special transfer of the lattice forces to the solid boundary.

The effect of varying l_{FEA} may be seen in figure 2 with three representative particles ranging from finely meshed to coarsely meshed. The finely meshed object ($l_{FEA} = 2.0$) gives a good object description and FEA deformation results, and the coarsely meshed object ($l_{FEA} = 6.2$) gives a poor object description and poor finite-element results. When l_{FEA} approaches dimensions below the lattice spacing, fewer links exist per finite-element surface. Thus, simple linear interpolation of link forces to the finite-element nodes on the intersecting surface may result in incorrect local surface stresses and, consequently, incorrect deformation. In order to correctly distribute the fluid–solid interactions to finely meshed objects, a secondary length scale, σ_F, is introduced through distribution weights. The link-wise force on the jth node is weighted according to

$$w_j = \exp\left(\frac{-d_j^2}{\sigma_F^2}\right), \tag{2.15}$$

where d_j is the distance between the link intersection with the finite-element surface and the jth finite-element node. The weights are normalized such that the sum of all weights for each lattice-link force is one. Buxton *et al.* (2005) use a similar scheme when transferring link forces to a discretized lattice-spring object, but they use a $1/d^2$ weighting scheme that fails when links land on a solid node. The distribution length scale, σ_F, controls the length scale for the fluid–solid interactions. For particles in which $l_{FEA} > 1$, the exponential decay closely approximates a straight linear interpolation to the adjacent FEA nodes. For particles where the solid mesh has a higher resolution than the fluid ($l_{FEA} < 1$), distribution according to (2.15) becomes necessary. In § 3.2, typical simulations with $l_{FEA} = 2.0$ and $D > 20$ are shown insensitive to changes in σ_F. Currently, all simulations have particles with $l_{FEA} > 1$, thus

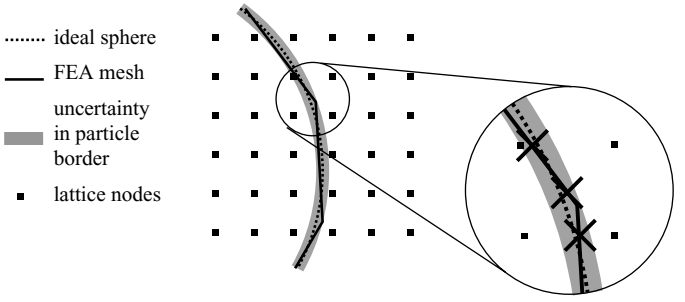

FIGURE 3. Uncertainty in the particle border created by the combined discretization of the solid and fluid. Discretization of the FEA mesh creates uncertainty in the particle border compared with an ideal sphere. This uncertainty is magnified by the overlay of the fluid lattice nodes and subsequent link finding shown in the inset. Link intersections are marked with crosses ($\times$).

linear interpolation is adequate. In the future, using smaller diameter particles may be possible, causing a decrease in l_{FEA} and requiring (2.15); however, the current method relies on the high fluid resolution to resolve lubrication in a link-wise manner.

2.5. *Near-contact interactions*

At high volume fractions, particles regularly approach within one lattice unit of each other. When no fluid node exists between two particles, sub-mesh modelling must be incorporated into the lattice-Boltzmann method. For the case of ideally smooth surfaces, Ding & Aidun (2003) develop a lubrication model extending the analytic solution for approaching spheres to a model for curved surfaces that uses lattice links. This model performs well for a variety of different particle radii and fluid viscosities; however, the required integration time step becomes very small as particles near contact. Implementing this lubrication model in the present FEA framework poses an additional problem. Particles can no longer be treated as idealized spheres, and the FEA discretization of the particle creates an artificial surface roughness that, as in the case of real particles, requires contact mechanics. Figure 3 shows the uncertainty in the particle border due to the FEA mesh as compared to an ideal smooth two-dimensional circular particle. This uncertainty is further compounded since the particle border is identified by intersections between lattice links and the FEA mesh (shown with crosses in the inset). For particles within this range of uncertainty, it is possible for the reported gap distance to fluctuate based on the underlying lattice-Boltzmann node locations – even to slightly negative values. Consequently, the results are unphysical at these gaps, and a contact model must be used to keep particles from entering this range.

The contact model developed uses a link-wise short-range exponential force similar to Buxton *et al.* (2005) to prevent particles from overlapping. In actual simulations, lubrication forces dominate and largely keep particles from approaching the contact regime. Deformation aids in this regard, because it allows the particles' surfaces to deform readily to avoid contact. This deformation creates flat spots on approaching particles, i.e. large areas of the particles are in close contact, and these areas have low curvatures. Consequently, the minimum gap between deformable particles as they pass one another is significantly larger than in rigid-particle suspensions. Near-contact

interactions along links connecting approaching solid surfaces are calculated as

$$dF_{\sigma i}^{(B)t+1} = \begin{cases} 0 & \text{if } g^{t+1} > c_{\sigma i}, \\ \left[\dfrac{3\bar{q}}{2c_{\sigma i}^2\lambda}\nu\rho\left(\dfrac{1}{(g^{t+1})^2} - \dfrac{1}{c_{\sigma i}^2}\right)\right]\boldsymbol{U}_{app}^{t+1}\cdot\boldsymbol{e}_{\sigma i} & \text{if } g_c < g^{t+1} < c_{\sigma i}, \\ \left[\dfrac{3\bar{q}}{2c_{\sigma i}^2\lambda}\nu\rho\left(\dfrac{1}{g_c^2} - \dfrac{1}{c_{\sigma i}^2}\right)\right]\boldsymbol{U}_{app}^{t+1}\cdot\boldsymbol{e}_{\sigma i} & \text{if } g^{t+1} < g_c \\ \quad + A_c\exp\left(\dfrac{-g^{t+1}+g_c}{\sigma_c}\right)\phi_{\sigma i}, & \end{cases} \tag{2.16}$$

where $\boldsymbol{U}_{app}^{t+1}$ is the surface approach velocity at time $t+1$, g^{t+1} is the link-wise gap between surfaces at time $t+1$, g_c is the contact cutoff distance, λ is the local surface curvature, and $\bar{q} = 0.6$ (Ding & Aidun 2003). These interactions are added to the approaching surfaces on both particles when the link-wise gap is less than the link length, $c_{\sigma i}$. Thus, the total force acting on a link connecting approaching surfaces is

$$F_{\sigma i}^{t+1} = F_{\sigma i}^{(B)t+1/2} + dF_{\sigma i}^{(B)t+1}, \tag{2.17}$$

where the link bounce-back force in (2.13) is written with a time superscript for the purposes of compactness. The contact force along a link is adjusted for friction by

$$\phi_{\sigma i} = \frac{(\boldsymbol{S}_N + \mu_{SF}\boldsymbol{S}_T)\cdot\boldsymbol{e}_{\sigma i}}{(\boldsymbol{S}_N + \boldsymbol{S}_T)\cdot\boldsymbol{e}_{\sigma i}}, \tag{2.18}$$

where $\boldsymbol{S}_N$ is the surface-normal vector, μ_{SF} is the coefficient of sliding friction, $\boldsymbol{S}_T$ is the projection of the surface-approach velocity on the surface tangential plane,

$$\boldsymbol{S}_T = \frac{\boldsymbol{S}_N \times \boldsymbol{U}_{app} \times \boldsymbol{S}_N}{|\boldsymbol{S}_N \times \boldsymbol{U}_{app} \times \boldsymbol{S}_N|}.$$

The appropriate contact scale in (2.16) is $A_c = 6\pi\mu R\tilde{U}$, where $\tilde{U}$ is the velocity scale of the problem in lattice units, e.g. $\dot{\gamma}R$ for particles in shear or the settling velocity for sedimentation problems. The contact cutoff distance, g_c, and the contact length scale, σ_c, are functions of the particle surface roughness and are determined *a priori*. The mean surface curvature in the lubrication model is the local curvature of the approaching finite-element surfaces, which is calculated by

$$\lambda = \frac{1}{N}\sum_{i=1}^{N}\left|\frac{\mathrm{d}\boldsymbol{T}_{surf}}{\mathrm{d}\boldsymbol{s}}\right|,$$

where $\boldsymbol{T}_{surf}$ is the tangent vector to the surface in the direction of $\boldsymbol{s}$, and $\boldsymbol{s}$ is a vector connecting finite-element surface centroids. The summation is performed over all neighbouring surfaces, with $N = 3$ for triangles.

The information needed to calculate $dF_{\sigma i}^{(B)t+1}$ in (2.16) is only known for time t, not $t+1$ as required for stability in Newmark's method (2.9). Using the variables $\boldsymbol{U}_{app}$ and g at time t leads to instability as deformable particles approach one another; however, the solution for $t+1$ variables requires the simultaneous solution of fluid–solid interactions and an inversion of the finite-element equation for every particle at every time step. This computation is too costly for the simulation of suspensions, and an iterative scheme is used to converge to the force at $t+1$. The lattice link forces are defined as

$$F_{\sigma i}^{t+1} = F_{\sigma i}^{(B)t+1/2} + dF_{\sigma i}^{(B)t} + \varepsilon_{F,\sigma i}^{t}, \tag{2.19}$$

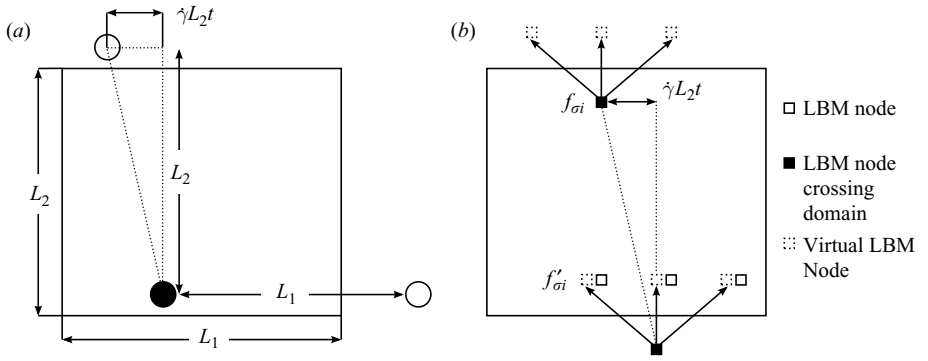

FIGURE 4. Illustrations of unbounded shear domain showing (*a*) solid particle and periodic images, and (*b*) wrapping of a representative LBM node.

where $dF_{\sigma i}^{(B)t}$ is defined as in (2.16) but using $\boldsymbol{U}_{app}$ and g at time t instead of $t+1$, and $\varepsilon_{F,\sigma i}^{t}$ is iterated to the correct numerical value.

2.6. *Unbounded shear domain*

To remove wall effects and enable the calculation of bulk rheological properties with fewer particles, an unbounded shear-periodic domain is implemented in the LBM framework through a Lees–Edwards boundary condition as described by Wagner & Pagonabarraga (2002). The flow and vorticity directions ($\boldsymbol{e}_1$ and $\boldsymbol{e}_3$, respectively) are treated in the usual periodic manner, with particle images reccurring at regular intervals according to L_1 and L_3, the flow and vorticity domain lengths. In the shear direction, $\boldsymbol{e}_2$, the periodic particle images convect with the shear velocity, such that the domain undergoes continuous shearing. Thus, a particle's image which is offset in the shear direction by L_2 will have a corresponding offset of $\dot{\gamma}L_2t$ in the flow direction. Figure 4(*a*) shows the relative position of a particle and its periodic images in unbounded shear; the vorticity direction, $\boldsymbol{e}_3$, is omitted for clarity. The velocity of the periodic image must also be adjusted; consequently, the component of the particle's velocity in the flow direction is altered by the domain speed, $\dot{\gamma}L_2$.

Implementing unbounded shear in the LBM framework poses unique challenges because the fluid is treated as a set of discrete particle distributions in a lattice arrangement. As shown in figure 4(*b*), the fluid distributions are subject to the same position and velocity adjustments as the particles, i.e. portions of the fluid distributions propagating outside the domain in the shear direction must have their location adjusted by L_2 in the shear direction and $\dot{\gamma}L_2t$ in the flow direction. Also, these fluid distributions must be altered to account for the jump in velocity via a Galilean transform applied to the portions of the fluid distribution crossing the domain in the shear direction. Following the notation of Wagner & Pagonabarraga (2002), this transform can be expressed as

$$f'_{\sigma i} = f_{\sigma i} + f_{\sigma i}^{(0)}(\boldsymbol{u}+\boldsymbol{U}) - f_{\sigma i}^{(0)}(\boldsymbol{u}),$$

where $f'_{\sigma i}$ is the fluid distribution adjusted for velocity $\boldsymbol{U}$, which in the case of simple shear is $\pm\dot{\gamma}L_2/2$. As an additional difficulty, the regular lattice arrangement is interrupted owing to the continuously time-varying nature of the flow-direction adjustment. Fluid distributions propagated across the domain must be stored in virtual fluid nodes and then interpolated to the neighbouring lattice nodes, also shown in figure 4(*b*).

2.7. *Stability*

Since the finite-element integration time scale is separate from the lattice time scale, it is possible for the boundary velocity to change on the lattice time scale and produce instability in the fluid–solid coupling shown in (2.13) and (2.14). Stability of the fluid–solid boundary coupling has been studied through analytic and numerical linear-perturbation analyses of a one-dimensional sample problem, in which the deformable solid boundary is modelled as a mass–spring–damper system, and the fluid is a semi-infinite one-dimensional lattice (MacMeccan 2007). The analytic solution for the movement of a mass–spring–damper system is known with characteristic parameters of the natural frequency, $\omega_n = \sqrt{k/m}$, damping ratio, $\zeta = b/2\sqrt{km}$, and damped natural frequency, $\omega_d = \omega_n\sqrt{1-\zeta^2}$, where k is the spring stiffness, m is the boundary mass, and b is the boundary damping. The resulting stability criteria is compared to a particle's finite-element frequency spectrum. For a given vibrational frequency, stability is achieved by restricting the lattice time step and adding minimal material damping into the finite-element model such that boundary velocity fluctuations do not occur on the lattice time scale.

3. Sample problems

In this section, several test problems are presented to demonstrate the effects of coupling the finite-element and lattice-Boltzmann methods for the simulation of particles in suspension. Of particular interest are the effects of particle discretization, l_{FEA}, on the lattice-Boltzmann method since they have not been studied previously. In order to investigate fluid–solid coupling, the following cases are presented: an inflated thin-walled sphere, a fluid-filled initially spherical membrane in shear flow, a settling particle, and red blood cell (RBC) deformation in flow chambers. Next, the case of two spheres approaching each other with constant velocity demonstrates the effect of l_{FEA} in lubrication and near-contact modelling. The effect of particle discretization on the calculation of the dilute limit stresslet is studied, and the suspension stress calculations are further validated by simulating a cubic array of spheres.

3.1. *Inflated sphere*

The inflated finite-element sphere in a quiescent fluid demonstrates the fluid–solid coupling between FEA and LBM. A thin-walled deformable sphere is subjected to an internal pressure by increasing the fluid density inside the particle and thus the lattice-Boltzmann pressure, which are related through $P = \rho_f c_s^2$, where ρ_f is the density of the fluid, and c_s is the lattice-Boltzmann pseudo-sound speed (here $c_s = 1/\sqrt{3}$). The pressure is applied through lattice links to the finite-element solid, and the external fluid is allowed to damp the solid motion. The resulting change in radius of the sphere is given by the analytic solution (Young & Budynas 2002),

$$\Delta R = \frac{P D^2 (1-\nu_p)}{8 E_Y t_M}, \tag{3.1}$$

where E_Y is Young's modulus, t_M is the wall thickness, and ν_p is Poisson's ratio. The computations are performed in a $100 \times 100 \times 100$ periodic domain, and the sphere's initial radius is set at 10 lattice units. Time-history results of the sphere's inflation are shown in figure 5 for three representative finite-element discretizations, where the finite-element discretizations are similar to those shown in figure 2. As seen in figure 5, the FEA model undergoes a damped oscillation when subjected to a step change in internal pressure. The period of the oscillation agrees with the analytic prediction of

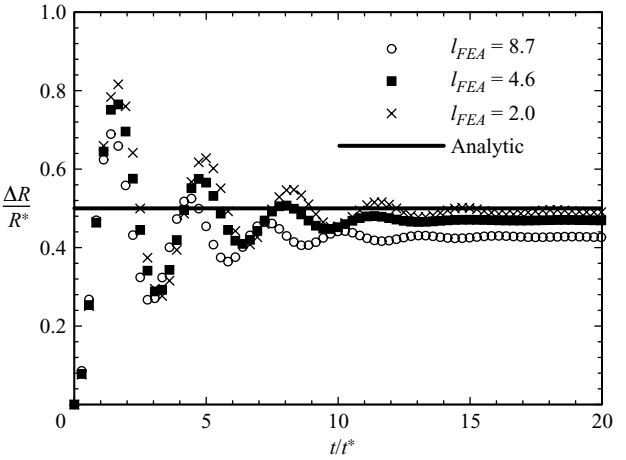

FIGURE 5. Transient response of finite-element thin-walled spheres in fluid which are inflated using the lattice pressure, $P = \rho_f c_s^2$; $R^* = PR^2(1-\nu_p)/E_Y t_M$, $t^* = R\sqrt{\rho_m/E_Y t_M}$.

a sphere *in vacuo*, calculated from (Buxton *et al.* 2005),

$$T = 2\pi R\left[\frac{2E_Y}{\rho_s(1-\nu_p)}\right]^{1/2},$$

where ρ_s is the density of the solid.

The results are also consistent with Buxton's results for an elastic lattice-spring sphere with internal fluid at a viscosity of 1/6. The present simulations were performed at a variety of particle orientations and positions, and the results show invariance with respect to rotation and translation. As seen in figure 5, the $l_{FEA} = 8.7$ particle produced oscillatory behaviour but failed to converge to the analytic result. This failure stems partly from the under-calculation of the lattice pressure owing to poor object description, and partly from the inaccurate finite-element solution of a poorly meshed object. Also seen in figure 5, results converge to the analytic solution for $l_{FEA} \leqslant 2.0$, while finite-element meshes of $l_{FEA} < 4.6$ produce less than 5 % error in the deformation results.

3.2. *Fluid-filled spherical capsule in shear flow*

The first-order analytic solution for a fluid-filled elastic and initially spherical membrane in shear flow, in which the sphere continuously deforms into an ellipse as it rotates, is given by (Barthès-Biesel & Sgaier 1985; Barthes-Biesel, Diaz & Dhenin 2002)

$$R_d^2 = R^2 + 5\frac{\mu_f R}{G_M}\frac{2+\nu_p}{1+\nu_p}\boldsymbol{r}\cdot\boldsymbol{E}\cdot\boldsymbol{r}, \tag{3.2}$$

where R_d is the deformed radius of the sphere, R is the undeformed radius, $\boldsymbol{r}$ is a spatial location on the surface of the ellipse, and $\boldsymbol{E}$ is the fluid rate-of-strain tensor. This solution is an asymptotic analysis on the capillary number and is valid for small deformations, $Ca_G \ll 1$. The lattice-Boltzmann finite-element method with linear-elastic shell elements produces behaviour consistent with this solution. The fluid-filled membrane continuously deforms as it rotates in shear flow, aligning 45° from the flow direction as predicted by (3.2).

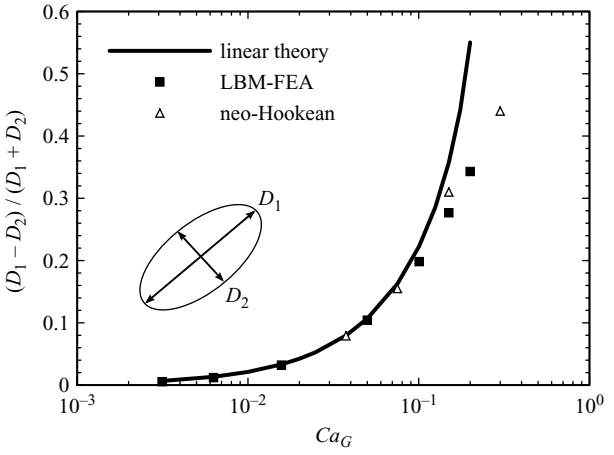

FIGURE 6. Comparison of membrane models for fluid-filled spherical capsules in shear flow. ($D = 20$ and $l_{FEA} = 2.0$) Small-deformation linear theory is valid for $Ca_G < 0.07$ (Barthès-Biesel & Sgaier 1985; Barthès-Biesel *et al.* 2002). Neo-Hookean membrane results are from Eggleton & Popel (1998).

The amount of deformation in the initially spherical particle is characterized by the major and minor diameters of the deformed shape. This deformation is plotted as a function of capillary number in figure 6 for the coupled LBM–FEA method compared with similar simulations using the immersed-boundary method with a nonlinear neo-Hookean membrane model (Eggleton & Popel 1998). In both the LBM–FEA and neo-Hookean results, the density and viscosity of the fluid inside and outside the particle are the same. The dilatational modulus of the membrane is three times the shear modulus for the neo-Hookean model and 2.96 times the shear modulus for the LBM–FEA simulations. For the simulations, the particle has $D = 20$ lattice units and $l_{FEA} = 2.0$. The linear theory in figure 6 is from (3.2) and is valid for $Ca_G \ll 1$ (Barthès-Biesel & Sgaier 1985). Good agreement is found between linear theory, LBM–FEA, and immersed-boundary for $Ca_G < 0.07$. Above the small-deformation limit ($0.07 < Ca_G < 0.25$), the linear finite-element model produces slight strain-hardening compared to the neo-Hookean model, as expected. Regardless, the amount of error introduced by the linear-elastic finite-element model is small compared to overall deformation, and valid results are expected using the linear model above the small-deformation limit.

Figure 7 shows the transient response for simulations of a spherical capsule at three capillary numbers, and the results are compared to linear theory and the neo-Hookean results from Eggleton & Popel (1998). As expected, good agreement between all theories is seen at lower capillary numbers, with divergence appearing at higher capillary numbers. Additionally, the effect of the force distribution length scale, σ_F, is shown, and the results are insensitive to changes in σ_F since $l_{FEA} = 2$. Therefore, suspension results shown in § 4 are insensitive to σ_F, and straight linear interpolation can be used to minimize computational time.

3.3. *Settling particle*

The case of a settling sphere in a square channel was thoroughly investigated by Aidun *et al.* (1998) for a smooth sphere in a lattice-Boltzmann fluid, and good agreement in settling velocity was found between lattice-Boltzmann simulations and experimental

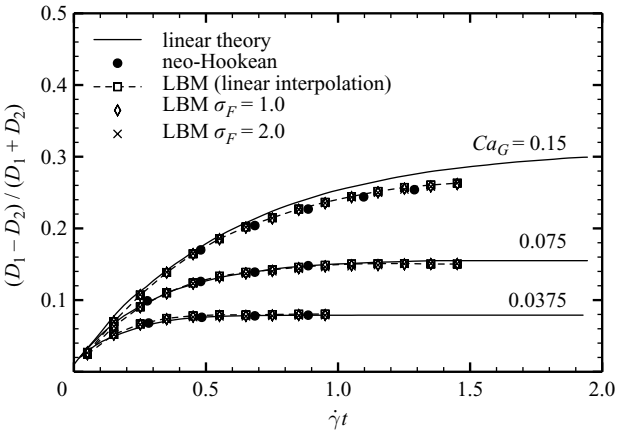

FIGURE 7. Transient response of a spherical capsule compared to linear theory and neo-Hookean results (Eggleton & Popel 1998). The effect of force distribution length scale, σ_F, on the deformation of a spherical capsule with $l_{FEA} = 2.0$ is negligible.

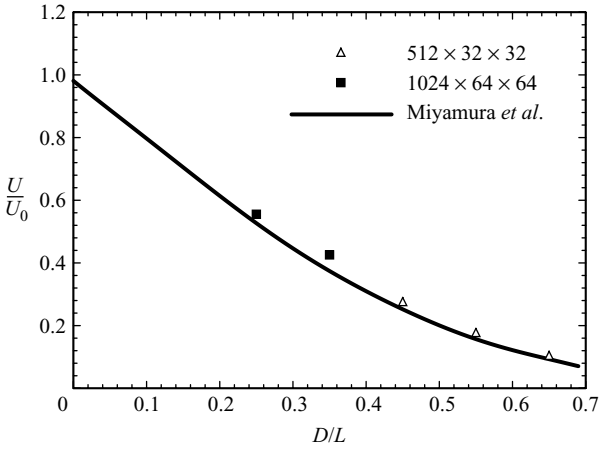

FIGURE 8. Settling on finite-element spheres with various mesh sizes in the centre of a square channel; $1.5 < l_{FEA} < 2.2$.

results by Miyamura, Iwasaki & Ishii (1981). Results are extended to rigid discretized finite-element spheres settling in a square channel in the same manner as Aidun, where the inlet velocity of the channel is set to zero and the particle is allowed to reach a steady-state terminal velocity starting from a position 200 lattice units from the inlet. Fluid domains subdivided into $512 \times 32 \times 32$ and $1024 \times 64 \times 64$ lattice units are tested, and particle diameter, D, to channel width, L, is varied from 0.15 to 0.65. The terminal velocity, U, is normalized by the unconstrained Stokes-flow solution, U_0, and the Reynolds number based on the unconstrained settling velocity for these simulations is 0.2. Results for various D/L are shown in figure 8 with $l_{FEA} < 2.2$ for all simulations. Again, good agreement is obtained with experiments for a variety of particle-diameter-to-channel-width ratios.

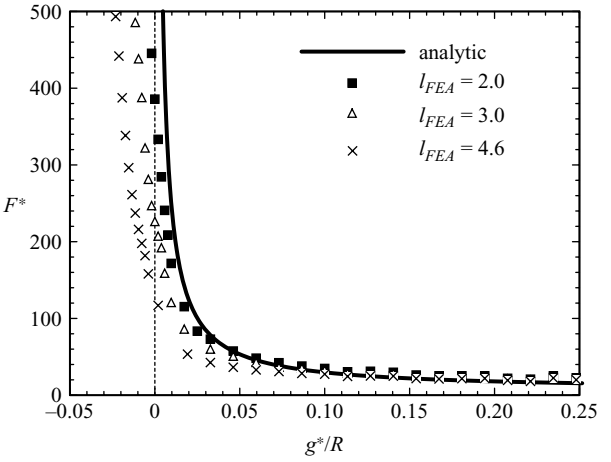

FIGURE 9. Spheres in a channel approaching with constant velocity. Channel walls are 70 units apart; the sphere radii are 10 units. Near-contact lubrication and contact mechanics are given by (2.16) with $\sigma_c = g_c = 0.02R$.

3.4. *Approaching spheres*

Effects of discrete finite-element particles on near-contact modelling are displayed in figure 9 for the case of two identical spheres approaching each other with constant velocity. Approaching spheres of different radii were also simulated and gave similar results. The simulations are similar to those presented by Ding & Aidun (2003) for lattice-link lubrication between smooth particles. Two spheres of $D = 20$ approach each other in a wall-bounded domain with walls 70 lattice-units apart, and to leading order, the lubrication force between the approaching spheres is given by (Cox 1974)

$$\frac{F_{lub}}{2\rho_f \nu \lambda^{-1} U_{app}} = \frac{3\pi}{4g^*\lambda} + C_{wall}, \tag{3.3}$$

where C_{wall} is a constant depending on the wall effects on drag, and g^* is the gap between spheres. It is important to note that g^* is the actual gap between ideal smooth spheres and not the gap as calculated by link intersections; consequently, the particles with poor object description have a large uncertainty in the location of the border as discussed in § 2.5, making small negative gaps possible. In these simulations, (2.16) is used for near-contact interactions with $\sigma_c = g_c = 0.02R$. Thus, the particle interactions are expected to diverge from (3.3) when $g^* < 0.02R$ as the modelling transitions from lubrication to contact modelling. As seen in figure 9, finely meshed spheres ($l_{FEA} = 2.0$) converge to the analytic lubrication solution at gaps above g_c. Conversely, particles with $l_{FEA} > 3.0$ under-predict lubrication forces and yield lower contact forces owing to poor object description in the link formation. Inaccurate local surface curvature calculations from poor object description partially explain the poor lubrication results, and these inadequacies pose significant problems for coarsely meshed particles in suspension. Also, the coarsely meshed particles have a large artificial surface roughness owing to poor object description, and particles exhibit surface roughness collisions and stick–slip-type dynamics when coupled to the under-predicted lubrication and contact forces. Thus, finite-element meshes having $l_{FEA} \leqslant 2.0$ are essential for simulating suspensions at high volume fraction.

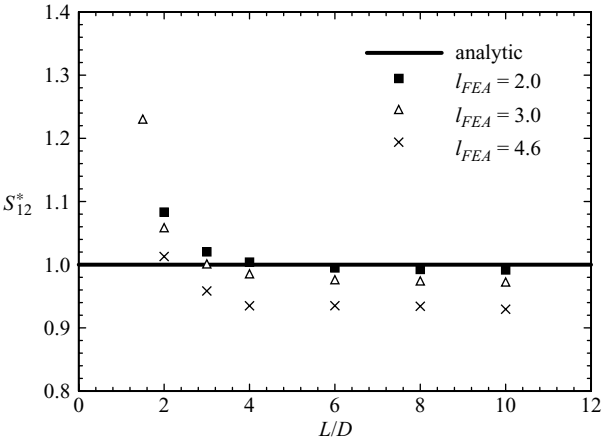

FIGURE 10. S_{12} component of stresslet normalized by $5/12\pi\mu D^3\dot{\gamma}$ for various domain sizes and particle discretizations.

3.5. *Bulk stress in the suspension*

When studying particle suspensions, describing the effect of suspended particles on rheology is accomplished by calculating the bulk stress in the suspension. The bulk stress is the volume-averaged stress of the suspending medium and the suspended particles. Following the method of Batchelor (1970) and neglecting inertial terms, the bulk stress, $\boldsymbol{\Sigma}$, can be separated into a Newtonian contribution due to the fluid and a potentially non-Newtonian contribution due to the particle, shown as

$$\boldsymbol{\Sigma} = 2\mu\boldsymbol{E} + \frac{1}{V}\sum \boldsymbol{S},$$

where $\boldsymbol{E}$ is the strain-rate tensor, and $\boldsymbol{S}$ is the contribution of an individual particle to the bulk stress known as the stresslet. The volume-averaged effect of all stresslets constitutes the contribution of the solid phase to the suspension stress. The stresslet for each particle is obtained via the surface integral

$$\boldsymbol{S} = \int_{A_0} \tfrac{1}{2}\left(\sigma \boldsymbol{x}_0 + \boldsymbol{x}_0\sigma\right)\cdot\boldsymbol{S}_N - \mu\left(\boldsymbol{u}_b\boldsymbol{S}_N + \boldsymbol{S}_N\boldsymbol{u}_b\right)\mathrm{d}A, \tag{3.4}$$

where σ is stress in the Newtonian suspending medium at the particle boundary, and $\boldsymbol{x}_0$ is the position relative to the centre of the particle.

For the coupled LBM–FEA method, this surface integral is readily computed since the stress on the surface of the particles is known via the fluid–solid coupling. Also, the boundary velocity used in the second term of the integral is known via the derivative of the finite-element deformation vector. The stresslet calculation is verified by simulating an isolated sphere in simple shear and comparing with the dilute-limit analytic result, shown as

$$\boldsymbol{S} = \tfrac{5}{6}\pi\mu D^3\boldsymbol{E}.$$

The dilute-limit behaviour remains Newtonian, and the only non-zero components of the stresslet are S_{12} and S_{21}, which, owing to the symmetric nature of the stresslet, are equivalent. The height of the shear channel is gradually increased to eliminate wall effects, and the S_{12} component of the stresslet normalized by the analytic result is shown in figure 10 for several particle discretizations. As the wall effects are removed, the stresslet converges to the analytic solution for $l_{FEA} < 3.0$ and $L/D > 4.0$.

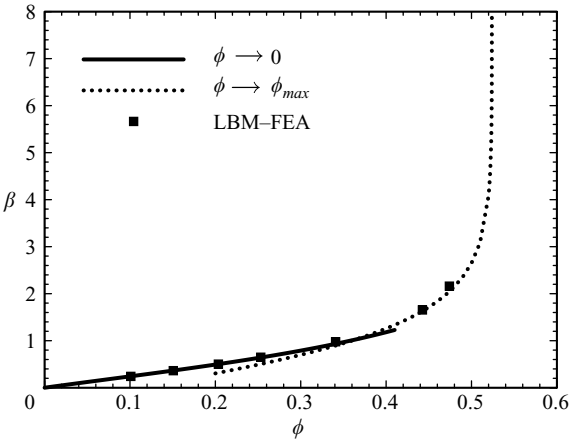

FIGURE 11. Variation of shear viscosity β parameter on particle volume fraction for periodic array of simple cubic spheres.

The suspension bulk-stress calculation and unbounded-shear-flow boundary condition were further validated by calculating the shear viscosities of a simple cubic array of spheres. For this validation, eight spheres are initialized into a simple cubic unit cell with fixed particle locations. A uniform shear field is applied via the Lees–Edwards boundary condition, and the particle and fluid phase relax to steady-state velocities. The calculated suspension stress is compared to analytic solutions for cubic lattices (Zuzovsky, Adler & Brenner 1983; Nunan & Keller 1984), in which the stress is expressed as a combination of two independent parameters, α and β. For rigid particles, α and β are functions of lattice geometry and volume fraction, and they correspond to pure straining and simple shear flow, respectively. The β parameter is shown in figure 11 for a simple cubic lattice at a variety of volume fractions. Also shown are asymptotic expansions given by Hofman, Clercx & Schram (2000) for low ϕ and $\phi \rightarrow \phi_{max}$, where ϕ is the particle volume fraction, and ϕ_{max} is the maximum packing ratio for the given cubic lattice. Good agreement is seen between the simulation results and asymptotic limits even at high volume fractions. The highest concentration simulation data ($\phi = 47\,\%$) corresponds to a gap between spheres of 0.7 lattice spacings, which is within the subgrid lubrication modelling shown in (2.16).

Although the Batchelor relation shown in (3.4) is strictly valid for Stokes flow, the simulations presented in §4 are at Reynolds numbers approaching the Stokes-flow limit (typically < 0.13). Dilute-limit work shows negligible inertial effects on the shear viscosity at these Reynolds numbers (Lin, Peery & Schowalter 1970; Mikulencak & Morris 2004), and simulations at lower Reynolds number give consistent results. Future work will attempt to quantify these inertial effects and to determine when they are significant.

3.6. *Red blood cell deformation*

Red blood cells consist of a cytoskeleton and phospholipid membrane encapsulating a fluid solution of haemoglobin. The primary structural protein of the cytoskeleton, spectrin, is loosely coupled to the fluid membrane through proteins such as ankyrin. This composite structure gives the RBC both solid and fluid properties. RBCs are often modelled using the nonlinear Skalak model (Skalak *et al.* 1973), which conserves RBC surface area, or a neo-Hookean model (Dao, Lim & Suresh 2003; Pozrikidis

2003; Bagchi, Johnson & Popel 2005), which does not conserve RBC surface area. The effect of the RBC membrane model is unknown for simulations of RBCs in high-volume-fraction suspensions. The present study is limited to simulations at small capillary number and models the RBC membrane using 504 linear-elastic finite-element 'shell' elements. In this section, this membrane model is compared to RBC deformation in flow chambers with excellent agreement. RBCs are modelled as three-dimensional biconcave elastic membranes encapsulating haemoglobin. The RBC membrane has an effective elastic shear modulus of 5.7×10^{-3} dyn cm^{-1} (Waugh & Evans 1979) and a bending stiffness of 2.2×10^{-12} dyn cm (Hwang & Waugh 1997). A Poisson ratio of 0.48 results in $E_Y/G_S = 2.96$ and similar behaviour to the neo-Hookean model for RBC membrane deformation. The haemoglobin inside the RBC membrane is set to a viscosity of 6 cP while the plasma surrounding the RBC has a viscosity of 1.2 cP at 37 °C (Harkness & Whittington 1970). The RBCs have a major diameter of 7.8 μm and thickness of 2.2 μm at the flank and 0.9 μm at the dimple. The major RBC diameter is set to 24 lattice units with an average $l_{FEA} = 2.0$.

Dilute-limit suspensions of RBCs in low-viscosity fluid and passing through a flow chamber provide an excellent opportunity to compare experimental RBC deformation to simulations. Conversely, many traditional experiments apply stresses much higher than arterial levels by using high-viscosity suspending fluid (Fischer, Stohr-Lissen & Schmid-Schonbein 1978; Bessis, Mohandas & Feo 1980; Schmid-Schonbein, Grebe & Heidtmann 1983; Watanabe *et al.* 2006). Furthermore, when RBCs are suspended in a high-viscosity fluid, they become oriented with the shear flow and exhibit a tank-treading motion (Fischer *et al.* 1978; Schmid-Schonbein *et al.* 1983). In the case of a low-viscosity suspending fluid, when shear stresses are below 1 N m^{-2}, many RBCs orient in the 'wheel' configuration, i.e. the symmetric axis of a RBC orients along the vorticity direction, which minimizes energy dissipation (Bitbol 1986). Although the preference for the 'wheel' orientation under these conditions is unclear, it requires both RBC deformation and fluid inertia. In this orientation, the thin flanks of the RBC support the shear stress, and the deformed RBC cross-sectional shape may be assumed elliptical and the major and minor axes measured. Liu *et al.* (2007) review this method. The RBC small-deformation index is given by

$$DI = \frac{D_1 - D_2}{D_1 + D_2}, \tag{3.5}$$

where D_1 and D_2 are the major and minor diameters of the RBC cross-section when viewed from the side. By assuming that the RBC shape is approximately elliptic, the deformation parameter is experimentally measured as

$$DI = \frac{(D_1/D_0)^2 - 1}{(D_1/D_0)^2 + 1}, \tag{3.6}$$

where D_0 is the average undeformed RBC diameter (Yao *et al.* 2001; Liu *et al.* 2007). Analysis of current LBM–FEA simulations indicates that (3.6) under predicts the small deformation index in (3.5) by only 1 %, validating the treatment of RBCs in the wheel orientation as deformed ellipses. In flow-chamber experiments, the small deformation index is directly observed through high-resolution photographs of RBCs.

The flow-chamber experiments of Yao *et al.* (2001) are simulated by placing a RBC in a rectangular flow chamber with a height of 45 μm. Increasing the pressure gradient varies the flow rate. As in experiments, the average shear stress in the chamber is

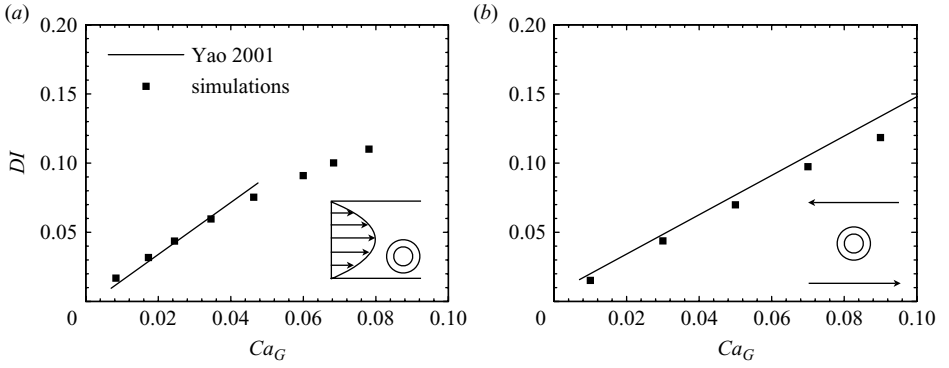

FIGURE 12. Small-deformation index for RBCs in 'wheel' orientation as a function of capillary number. In both plots, the suspending fluid has a viscosity of 0.707 cP. (*a*) Results for flow chamber of height 45 μm with RBC located at 1/4 of the flow chamber height. Experimental flow-chamber results are from Yao *et al.* (2001). (*b*) Results for shear flow. Experimental results are from Yao *et al.* (2001) using low-viscosity ektacytometry.

measured from the volumetric flow rate, Q, as

$$\bar{\tau} = \frac{3Q\mu_f}{h^2 w}, \tag{3.7}$$

where μ_f is the viscosity of the suspending fluid (0.707 cP), h is the height of the chamber (45 μm), and w is the width of the chamber. The RBCs distance from the wall and, consequently, the average shear stress experienced are unknown in the experiments. Thus, in the simulations, the RBC is placed at 1/4 of the height of the flow chamber where the average shear stress is found. RBCs reach steady-state deformation quickly ($\dot{\gamma}t < 2$) and thus do not move significantly from this position. The experimental flow chamber has a length of 6.5 cm and a width of 1 cm to avoid entrance and transverse wall effects. The length and width of the simulations are set to periodic boundaries and dimensions of 90 μm and 45 μm, respectively. Increasing the length and width of the simulations by three times produces negligible changes in RBC deformation, verifying the size of the computational domain.

The RBC's small-deformation parameter is shown in figure 12(*a*) as a function of capillary number. Simulations agree well with experimental results; however, the slope of the experimental regression is slightly larger than the simulation results owing to uncertainty in RBC material properties and RBC distance from the wall in experiments. At shear stresses above experimental results, RBCs took longer to reach steady-state deformation and started to precess away from the 'wheel' orientation. Thus, the RBCs at higher shear stress resulted in slightly lower deformation than linear deformation would indicate.

Low-viscosity ektacytometry measures RBC deformations in shear flow though changes in laser-diffraction patterns. Low volume fractions of RBCs are suspended in a low-viscosity fluid and placed in a Couette device, in which inner and outer rotating cylinders cause shear flow. Owing to the low-viscosity suspending fluid, many RBCs orient in the 'wheel' configuration as discussed above. The deformations observed in low-viscosity ektacytometry have been validated to the flow chamber technique described in Yao *et al.* (2001) and Liu *et al.* (2007) and to other experimental measures of RBC elasticity such as micropipette aspiration (Liu *et al.* 2007). Computational comparisons to low-viscosity ektacytometry are performed by placing a RBC in

wall-bounded shear flow with the walls separated by four RBC diameters. The viscosity of the suspending fluid is 0.707 cP. The RBC small-deformation parameter is shown in figure 12(*b*) as a function of capillary number with the simulations agreeing well with experiments at all shear stresses.

4. Suspension results

The newly developed LBM–FEA method is capable of simulating suspensions of red blood cells (RBCs) and platelets at 40 % volume fraction. The LBM–FEA method is particularly well-suited to simulate blood flow because RBC deformation is one of the most important aspects of blood rheology. Changes in RBC deformation are known to alter continuum-level measures of suspension viscosity (Kim & Beissinger 1993; Shin *et al.* 2004) and diffusivity (Cha & Beissinger 1996). Furthermore, the stress environment in whole blood is known to be important in a range of problems such as leukocyte and platelet adhesion (Munn *et al.* 1996; Konstantopoulos, Kukreti & McIntire 1998; Sun, Migliorini & Munn 2003).

RBCs are modelled as three-dimensional biconcave elastic membranes encapsulating haemoglobin, as described in § 3.6, with the major diameter set to 24 lattice units and an average $l_{FEA} = 2.0$. Platelets are also included in simulations to show the versatility of the LBM–FEA method. Unlike RBCs, platelets have a complex internal structure consisting of a complex cytoskeleton which contains dense bodies and α-granules. Platelets are modelled as an effective solid using 711 linear-elastic 'brick-type' finite-elements with a Young's modulus of $1.7 \times 10^3\,\mathrm{dyn\,cm^{-2}}$ and shear modulus of $0.57 \times 10^3\,\mathrm{dyn\,cm^{-2}}$ (Haga *et al.* 1998). Although platelet deformation is small compared with RBCs, the inclusion of a finite-element representation of platelets has negligible computational penalty owing to their small numbers as compared with RBCs. The inactivated platelets simulated in this work have an approximately ellipsoidal shape with a major diameter of 2.5 μm and a thickness of 0.7 μm (Paulus 1975; Haga *et al.* 1998), and they account for 0.1 % of the total volume fraction. Owing to their smaller size, platelets are meshed with an average $l_{FEA} = 1.5$.

4.1. *Suspension viscosity*

For the purposes of studying blood rheology at continuum-level scales, suspensions of RBCs and platelets are simulated in unbounded shear flow at 40 % volume fraction and $Ca_G = 0.037$. In these simulations, the length of the domain in the shear and flow directions is 1.5 times the length in the vorticity direction. The reduced viscosity of blood is shown as a function of the number of simulated RBCs in figure 13 with

$$\mu_r = \frac{\mu_{eff}}{\mu},$$

where μ_{eff} is the effective suspension viscosity, and μ is the viscosity of the suspending medium. In figure 13, the time-averaged relative viscosity is plotted against non-dimensional time to show convergence of viscosity and insensitivity to the number of particles. Microstructure such as RBC orientation was also consistent between simulations above 73 RBCs. These results differ from simulations of wall-bounded suspensions in shear flow where the suspension viscosity decreases with gap height when the gap height is greater than the RBC diameter (MacMeccan 2007). A depletion layer forms near the wall, reducing the viscosity locally. Thus, the reported viscosity in wall-bounded simulations is lower than simulations where wall effects are negligible.

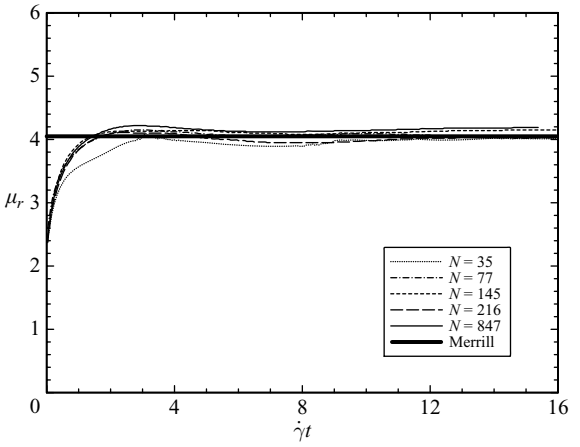

FIGURE 13. Time-averaged effective suspension viscosity for RBCs and platelets at $\phi = 40.5\,\%$ and $Ca_G = 0.037$ for various number of particles, N. Experimental whole blood results are from Merrill *et al.* (1963).

4.2. *Shear-thinning behaviour*

The shear-dependent nature of blood rheology at continuum scales is well-documented with non-Newtonian shear-thinning viscosity in Couette-type viscometers with a large gap (Merrill *et al.* 1963; Brooks, Goodwin & Seaman 1970). To study the shear-dependence of blood, 204 RBCs and 12 platelets are simulated in unbounded shear at 40 % volume fraction with $0.011 < Ca_G < 0.047$ for the RBCs, corresponding to shear rates ranging between 15 s^{-1} and 64 s^{-1}, respectively. The shear-dependent behaviour of blood at $Ca_G < 0.01$ is not investigated owing to the influence of non-hydrodynamic particle interactions that lead to RBC aggregates known as rouleaux (Fung 1993). Simulations are performed at $Re_p = 0.1$ and a lattice-Boltzmann Mach number of 0.03. Simulation results at $Re_p = 0.03$ and $Re_p = 0.2$ show insensitivity to changes in particle Reynolds number. Comparisons between simulations and experiments are made based on RBC Ca_G similarity. An example RBC simulation at $\dot{\gamma}t = 0$ and $\dot{\gamma}t = 10$ is shown in figure 14(a, b) with steady-state suspension dynamics reached by $\dot{\gamma}t = 10$. As seen in figure 14(a), RBCs are initialized at random locations and orientations, using a procedure described in MacMeccan (2007).

At the investigated shear rates and 40 % volume fraction, blood is often described by Casson's equation,

$$\sqrt{\tau_{eff}} = \sqrt{\tau_{yield}} + C\sqrt{\dot{\gamma}},$$

where τ_{eff} is the effective suspension shear stress, and τ_{yield} is a constant which is the yield stress of the suspension in shear. A Casson fluid exhibits non-Newtonian and shear-thinning behaviour. The reduced viscosity of blood is shown as a function of Ca_G in figure 15. In dimensional values, the effective viscosity in simulations decreases from 5.46 cP at $Ca_G = 0.011$ to 4.73 cP at $Ca_G = 0.047$. The simulations shown agree well with experimental values reported by Merrill *et al.* (1963) for blood at 42.5 % volume fraction in a large-gap Couette-type viscometer. Experimental blood flow data reported by Fung (1993) at higher and lower volume fraction–display a larger and smaller viscosity, respectively, with Ca_G similarity based on material properties at 25 °C (Harkness & Whittington 1970; Waugh & Evans 1979). Good agreement between simulations and experimental data indicates that the LBM–FEA method

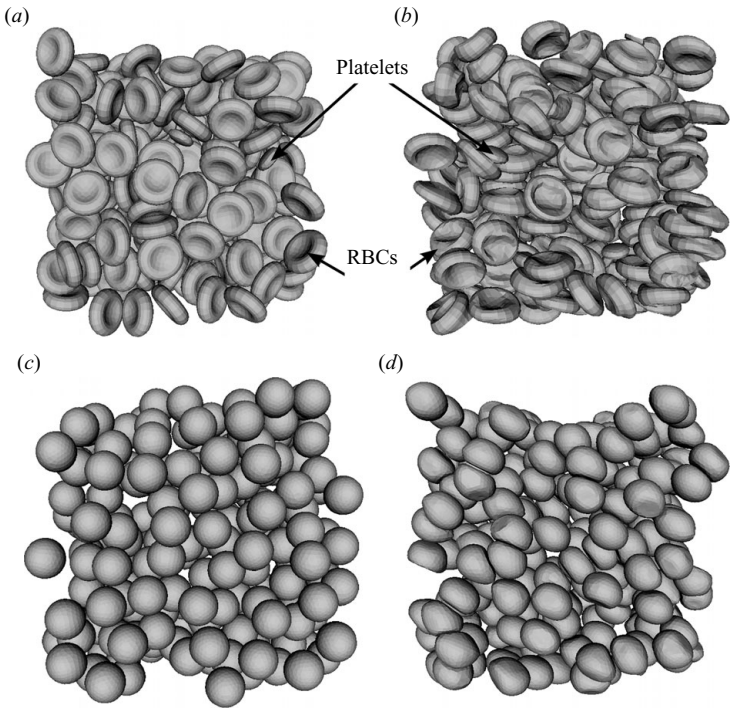

FIGURE 14. Example simulations: (a, b) 204 RBCs with $Ca_G = 0.022$ and 12 platelets in unbounded shear flow at (a) $\dot{\gamma}t = 0$ and (b) $\dot{\gamma}t = 10$. (c, d) 200 fluid-filled capsules with $Ca_G = 0.027$ in unbounded shear flow at (c) $\dot{\gamma}t = 0$ and (d) $\dot{\gamma}t = 10$.

developed in this work contains the necessary physics to predict blood behaviour at physiologic haematocrit and shear rates. Furthermore, the RBC membrane model, which is consistent with published models, is appropriate for the simulation of RBC suspensions at low to moderate shear rates. Further work is required to investigate the effect of Skalak and neo-Hookean RBC membrane models on blood rheology and microstructure, especially at higher shear rates where the models diverge owing to increased membrane strain. Owing to the versatility of the finite-element framework, these models may easily be incorporated into this methodology.

Also shown in figure 15 are results for 200 fluid-filled and initially spherical capsules simulated at 40 % volume fraction in unbounded shear flow, with capsule membrane properties that are identical to RBC membranes. The fluid viscosity inside the capsule is that of haemoglobin. An example simulation at $\dot{\gamma}t = 0$ and $\dot{\gamma}t = 10$ is shown in figure 14(c, d) with steady-state suspension dynamics reached by $\dot{\gamma}t = 10$. Suspensions of spherical capsules display shear-thinning behaviour similar to suspensions of biconcave RBCs; however, values of μ_r are significantly lower in suspensions of spherical capsules than in suspensions of biconcave RBCs. Thus, suspensions of spherical capsules are not an optimal analogue for studying for blood rheology.

4.3. *Concentration-dependent behaviour*

In addition to shear-thinning rheology, the LBM–FEA method can probe the concentration dependence of blood viscosity as seen in figure 16. The RBCs in all simulations have a capillary number of 0.021, and the domain size is fixed while the number of particles varies from 54 to 216. The LBM–FEA method accurately predicts

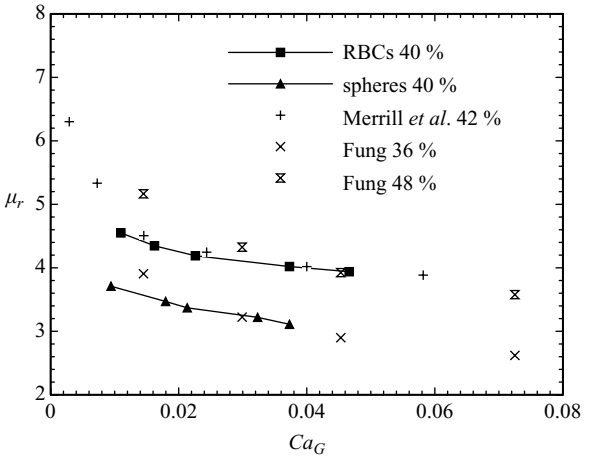

FIGURE 15. Reduced suspension viscosity of simulations of 204 RBCs and 12 platelets at 40 % volume fraction and 200 fluid-filled spherical capsules at 40 % volume fraction in unbounded shear flow as a function of Ca_G. Experimental data reported by Merrill *et al.* (1963) and Fung (1993) are for blood in a Couette-type viscometer with a large gap.

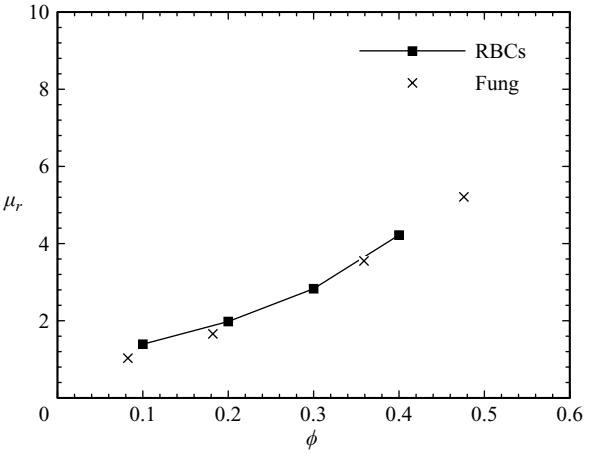

FIGURE 16. Reduced suspension viscosity of simulations of blood at different volume fractions and $Ca_G = 0.021$ compared to experimental results by Fung (1993) for blood in a Couette-type viscometer with a large gap.

the concentration-dependent viscosity of blood at physiologic volume fraction, while slightly over predicting viscosity at low volume fraction. The slight over prediction at low volume fraction is most likely to be due to experimental and biological variation, in particular, reported physical parameters for non-dimensional results. The accurate description of blood at varying concentrations is particularly important for the simulation of complex flows where RBC migration drives concentration gradients.

5. Conclusions

A coupled lattice-Boltzmann–finite-element method has been developed for the direct numerical simulation of suspensions of large numbers of deformable particles.

The LBM–FEA method is capable of quantitatively describing RBC deformation and suspension rheology at continuum-level length scales, i.e. at lengths much larger than the suspended particles. This method captures both shear-thinning and concentration-dependent behaviours. Additionally, no open parameters were used to match simulation results to experimental results, since all pertinent physics are explicitly included in the method. Unlike Stokesian dynamics or the boundary-integral method, the LBM–FEA method scales linearly with the number of particles at a given volume fraction and better than linearly with the number of particles at a given domain size. Additionally, the local nature of the LBM and particle dynamics allows for significant parallelism.

The LBM–FEA method is valid for solid deformable particles such as fibres or fluid-filled capsules such as red blood cells and liposomes. Deformable particles may have a different density from the fluid, and the internal fluid of a fluid-filled capsule may have a different viscosity from the external fluid with no computational penalty. Different particle shapes may be simulated by simply meshing differently shaped objects, and active motion of the particles may be prescribed such as pseudopod formation in activated platelets. Thus, the LBM–FEA method is extremely versatile and powerful for a variety of applications.

Although the method presented here is efficient only for particle Reynolds numbers $O(0.01-1.0)$, other lattice-Boltzmann techniques may be substituted for zero (Ding & Aidun 2008) or high (Lallemand & Luo 2000) Reynolds-number flows. One current limitation to the method is the increased computational time experienced when incorporating nonlinear solid material properties, owing to the small lattice-Boltzmann time scale. To address this limitation, a nonlinear finite-element model based on the continuum time scale is currently being developed.

REFERENCES

Aidun, C. K. & Lu, Y. 1995 Lattice Boltzmann simulation of solid particles suspended in fluid. *J. Stat. Phys.* **81**, 49–61.

Aidun, C. K., Lu, Y. & Ding, E. J. 1998 Direct analysis of particulate suspensions with inertia using the discrete Boltzmann equation. *J. Fluid Mech.* **373**, 287–311.

Bagchi, P., Johnson, P. C. & Popel, A. S. 2005 Computational fluid dynamic simulation of aggregation of deformable cells in a shear flow. *J. Biomech. Engng* **127**, 1070.

Barthès-Biesel, D. & Sgaier, H. 1985 Role of membrane viscosity in the orientation and deformation of a spherical capsule suspended in shear flow. *J. Fluid Mech.* **160**, 119–135.

Barthès-Biesel, D., Diaz, A. & Dhenin, E. 2002 Effect of constitutive laws for two-dimensional membranes on flow-induced capsule deformation. *J. Fluid Mech.* **460**, 211–222.

Batchelor, G. K. 1970 The stress system in a suspension of force-free particles. *J. Fluid Mech.* **41**, 545–570.

Bathe, K. J. 1996 *Finite Element Procedures*. Prentice-Hall.

Bessis, M., Mohandas, N. & Feo, C. 1980 Automated ektacytometry: a new method of measuring red cell deformability and red cell indices. *Blood Cells* **6**, 315–327.

Bitbol, M. 1986 Red blood cell orientation in orbit C = 0. *Biophys. J.* **49**, 1055–1068.

Brady, J. F. & Bossis, G. 1988 Stokesian dynamics. *Annu. Rev. Fluid Mech.* **20**, 111–157.

Breyiannis, G. & Pozrikidis, C. 2000 Simple shear flow of suspensions of elastic capsules. *Theor. Comput. Fluid Dyn.* **13**, 327–347.

Brooks, D. E., Goodwin, J. W. & Seaman, G. V. 1970 Interactions among erythrocytes under shear. *J. Appl. Physiol.* **28**, 172–177.

Buxton, G. A., Verberg, R., Jasnow, D. & Balazs, A. C. 2005 Newtonian fluid meets an elastic solid: coupling lattice Boltzmann and lattice-spring models. *Phys. Rev.* E **71**, 56707.

Campanelli, M., Berzeri, M. & Shabana, A. A. 2000 Performance of the incremental and non-incremental finite element formulations in flexible multibody problems. *J. Mech. Design* **122**, 498.

Cha, W. & Beissinger, R. L. 1996 Augmented mass transport of macromolecules in sheared suspensions to surfaces b. bovine serum albumin. *J. Colloid Interface Sci.* **178**, 1–9.

Chen, S. & Doolen, G. D. 1998 Lattice Boltzmann method for fluid flows. *Annu. Rev. Fluid Mech.* **30**, 329–364.

Cohu, O. & Magnin, A. 1995 Rheometry of paints with regard to roll coating process. *J. Rheol.* **39**, 767.

Cox, R. G. 1974 The motion of suspended particles almost in contact. *Intl J. Multiphase Flow* **1**, 343–371.

Dao, M., Lim, C. T. & Suresh, S. 2003 Mechanics of the human red blood cell deformed by optical tweezers. *J. Mech. Phys. Solids* **51**, 2259–2280.

Ding, E. J. & Aidun, C. K. 2000 The dynamics and scaling law for particles suspended in shear flow with inertia. *J. Fluid Mech.* **423**, 317–344.

Ding, E. J. & Aidun, C. K. 2003 Extension of the lattice-Boltzmann method for direct simulation of suspended particles near contact. *J. Stat. Phys.* **112**, 685–708.

Ding, E. J. & Aidun, C. K. 2006 Cluster size distribution and scaling for spherical particles and red blood cells in pressure-driven flows at small Reynolds number. *Phys. Rev. Lett.* **96**, 204502.

Dupin, M. M., Halliday, I., Care, C. M., Alboul, L. & Munn, L. L. 2007 Modeling the flow of dense suspensions of deformable particles in three dimensions. *Phys. Rev.* E **75**, 66707.

Eggleton, C. D. & Popel, A. S. 1998 Large deformation of red blood cell ghosts in a simple shear flow. *Phys. Fluids* **10** (8), 1834–1845.

Fischer, T. M., Stohr-Lissen, M. & Schmid-Schonbein, H. 1978 The red cell as a fluid droplet: tank tread-like motion of the human erythrocyte membrane in shear flow. *Science* **202**, 894–896.

Fung, Y. 1993 *Biomechanics: Mechanical Properties of Living Tissues*. Springer.

Goddard, J. D. & Miller, C. 1967 Nonlinear effects in the rheology of dilute suspensions. *J. Fluid Mech.* **28**, 657–673.

Goldsmith, H. L., Bell, D. N., Braovac, S., Steinberg, A. & McIntosh, F. 1995 Physical and chemical effects of red cells in the shear-induced aggregation of human platelets. *Biophys. J.* **69**, 1584–1595.

Haga, J. H., Beaudoin, A. J., White, J. G. & Strony, J. 1998 Quantification of the passive mechanical properties of the resting platelet. *Ann. Biomed. Engng* **26**, 268–277.

Harkness, J. & Whittington, R. B. 1970 Blood-plasma viscosity: an approximate temperature-invariant arising from generalised concepts. *Biorheology* **6** (3), 169–187.

Hofman, J. M. A., Clercx, H. J. H. & Schram, P. 2000 Effective viscosity of dense colloidal crystals. *Phys. Rev.* E **62**, 8212–8233.

Hwang, W. C. & Waugh, R. E. 1997 Energy of dissociation of lipid bilayer from the membrane skeleton of red blood cells. *Biophys. J.* **72**, 2669–2678.

Kim, D. & Beissinger, R. L. 1993 Augmented mass transport of macromolecules in sheared suspensions to surfaces. *J. Colloid Interface Sci.* **159**, 9–20.

Konstantopoulos, K., Kukreti, S. & McIntire, L. V. 1998 Biomechanics of cell interactions in shear fields. *Adv. Drug Delivery Rev.* **33**, 141–164.

Kroll, M. H., Hellums, J. D., McIntire, L. V., Schafer, A. I. & Moake, J. L. 1996 Platelets and shear stress. *Blood* **88**, 1525–1541.

Ladd, A. J. C. 1994 Numerical simulations of particulate suspensions via a discretized Boltzmann equation. Part 1. Theoretical foundation. *J. Fluid Mech.* **271**, 285–309.

Ladd, A. J. C. & Verberg, R. 2001 Lattice-Boltzmann simulations of particle–fluid suspensions. *J. Stat. Phys.* **104**, 1191–1251.

Lallemand, P. & Luo, L. S. 2000 Theory of the lattice Boltzmann method: dispersion, dissipation, isotropy, Galilean invariance, and stability. *Phys. Rev.* E **61**, 6546–6562.

Lin, C. J., Peery, J. H. & Schowalter, W. R. 1970 Simple shear flow round a rigid sphere: inertial effects and suspension rheology. *J. Fluid Mech.* **44**, 1–17.

Liu, X., Tang, Z., Zeng, Z., Chen, X., Yaob, W., Yana, Z., Shic, Y., Shand, H., Sun, D., Hee, D. & Wen, Z. 2007 The measurement of shear modulus and membrane surface viscosity of RBC membrane with ektacytometry: a new technique. *Math. Biosci.* **209**, 190–204.

Liu, Y. & Liu, W. K. 2006 Rheology of red blood cell aggregation by computer simulation. *J. Comput. Phys.* **220**, 139–154.

MacMeccan, R. 2007 Mechanistic effects of erythrocytes on platelet deposition in coronary thrombosis. PhD thesis, Georgia Institute of Technology.

McNamara, G. R. & Zanetti, G. 1988 Use of the Boltzmann equation to simulate lattice-gas automata. *Phys. Rev. Lett.* **61**, 2332–2335.

Merrill, E. W., Cokelet, G. C., Britten, A. & Wells, R. 1963 Non-Newtonian rheology of human blood-effect of fibrinogen deduced by 'subtraction'. *Circ. Res.* **13**, 48–55.

Mikulencak, D. R. & Morris, J. F. 2004 Stationary shear flow around fixed and free bodies at finite Reynolds number. *J. Fluid Mech.* **520**, 215–242.

Miyamura, A., Iwasaki, S. & Ishii, T. 1981 Experimental wall correction factors of single solid spheres in triangular and square cylinders, and parallel plates. *Intl J. Multiphase Flow* **7**, 41–46.

Möller, T. & Trumbore, B. 1997 Fast, minimum storage ray-triangle intersection. *J. Graphics Tools* **2**, 21–28.

Munn, L. L., Melder, R. J. & Jain, R. K. 1996 Role of erythrocytes in leukocyte–endothelial interactions: mathematical model and experimental validation. *Biophys. J.* **71**, 466–478.

Nunan, K. C. & Keller, J. B. 1984 Effective viscosity of a periodic suspension. *J. Fluid Mech.* **142**, 269–287.

Pal, R. 2003 Rheology of concentrated suspensions of deformable elastic particles such as human erythrocytes. *J. Biomech.* **36**, 981–9.

Paulus, J. M. 1975 Platelet size in man. *Blood* **46**, 321–336.

Pozrikidis, C. 2003 Numerical simulation of the flow-induced deformation of red blood cells. *Ann. Biomed. Engng* **31**, 1194–1205.

Pozrikidis, C. 2005 Numerical simulation of cell motion in tube flow. *Ann. Biomed. Engng* **33**, 165–178.

Qi, D. 1999 Lattice-Boltzmann simulations of particles in non-zero-Reynolds-number flows. *J. Fluid Mech.* **385**, 41–62.

Rankin, C. C. & Brogan, F. A. 1986 An element independent corotational procedure for the treatment of large rotations. *Trans. ASME J. Press. Vessel Technol. ASME* **108**, 165–174.

Schmid-Schonbein, H., Grebe, R. & Heidtmann, H. 1983 A new membrane concept for viscous rbc deformation in shear: spectrin oligomer complexes as a Bingham-fluid in shear and a dense periodic colloidal system in bending. *Ann. NY Acad. Sci.* **416**, 225–254.

Shin, S., Ku, Y., Park, M. S. & Suh, J. S. 2004 Measurement of red cell deformability and whole blood viscosity using laser-diffraction slit rheometer. *Korea-Aust. Rheol. J.* **16**, 85–90.

Sierou, A. & Brady, J. F. 2002 Rheology and microstructure in concentrated noncolloidal suspensions. *J. Rheol.* **46**, 1031–1056.

Sierou, A. & Brady, J. F. 2004 Shear-induced self-diffusion in non-colloidal suspensions. *J. Fluid Mech.* **506**, 285–314.

Skalak, R., Tozeren, A., Zarda, R. P. & Chien, S. 1973 Strain energy function of red blood cell membranes. *Biophys J.* **13**, 245.

Sun, C., Migliorini, C. & Munn, L. L. 2003 Red blood cells initiate leukocyte rolling in postcapillary expansions: a lattice Boltzmann analysis. *Biophys. J.* **85**, 208–222.

Thorp, B. A. & Kocurek, M. J. 1998 *Pulp and Paper Manufacture. Volume 7, Paper Machine Operations*. Technical Section, Canadian Pulp and Paper Association, Montreal, Quebec.

Wagner, A. J. & Pagonabarraga, I. 2002 Lees–Edwards boundary conditions for lattice Boltzmann. *J. Stat. Phys.* **107**, 521–537.

Watanabe, N., Kataoka, H., Yasuda, T. & Takatani, S. 2006 Dynamic deformation and recovery response of red blood cells to a cyclically reversing shear flow: effects of frequency of cyclically reversing shear flow and shear stress level. *Biophys. J.* **91**, 1984.

Waugh, R. & Evans, E. A. 1979 Thermoelasticity of red blood cell membrane. *Biophys. J.* **26**, 115–131.

Yao, W., Wen, Z., Yan, Z., Sun, D., Ka, W., Xie, L. & Chien, S. 2001 Low viscosity ektacytometry and its validation tested by flow chamber. *J. Biomech.* **34**, 1501–1509.

Young, W. C. & Budynas, R. G. 2002 *Roark's Formulas for Stress and Strain*. McGraw-Hill.

Zinchenko, A. Z. & Davis, R. H. 2002 Shear flow of highly concentrated emulsions of deformable drops by numerical simulations. *J. Fluid Mech.* **455**, 21–62.

Zuzovsky, M., Adler, P. M. & Brenner, H. 1983 Spatially periodic suspensions of convex particles in linear shear flows. III. Dilute arrays of spheres suspended in Newtonian fluids. *Phys. Fluids* **26**, 1714.